Radar Studies of Comet Nuclei and Grain Comae

John K. Harmon and Michael C. Nolan
Arecibo Observatory

Steven J. Ostro
Jet Propulsion Laboratory, California Institute of Technology

Donald B. Campbell
Cornell University

A close-approaching comet can show detectable echoes from its nucleus, or from large coma grains, or both. Nine comets have been detected since 1980 with the Arecibo and Goldstone radars; this includes six nucleus detections and five grain-coma detections. The nucleus radar cross sections span a large range of values consistent with a factor-of-10 range of nucleus sizes. Comparisons with independent size estimates for these comets support this size range and give radar albedos of 0.04–0.1, which is about half the typical asteroid radar albedo. The albedos correspond to nucleus surface densities ~0.5–1.5 g/cm^3. Coma echo models based on simple grain ejection theories can explain the radar cross sections using reasonable grain size distributions that include a substantial population of centimeter-sized grains; in one case there is evidence for a cutoff in the size distribution consistent with a gravity-limited maximum liftable grain size. The models indicate that some comets emit large grains at rates (~10^6 g/s) that are comparable with their gas and dust production rates. The primary goal of cometary radar is to obtain delay-Doppler images of a nucleus. Eleven short-period comets are potentially detectable over the next two decades, a few of which may be suitable for imaging. These could be supplemented by chance close apparitions of new comets.

1. INTRODUCTION

When the comet radar chapter by *Kamoun et al.* (1982a) was written for the first *Comets* book (*Wilkening,* 1982), only one comet, 2P/Encke, had been detected by radar. Since then, eight more comet detections have been made with the Arecibo and Goldstone radars (Table 1). While few in number, owing to the rarity of close comet approaches, these detections have been sufficient to establish comets as interesting and diverse radar targets.

The Encke detection of 1980 (*Kamoun et al.,* 1982a,b; *Kamoun,* 1983) showed a narrow Doppler spike consistent with backscatter from a solid rotating nucleus a few kilometers in size. Subsequent nucleus detections of other comets have been similar in character, but show differences in radar cross section consistent with an order-of-magnitude range of nucleus sizes. In principle, delay-Doppler radar imaging can determine the size, shape, rotation, and radar albedo of a nucleus unambiguously, as is being done for an increasing number of asteroids. Since no delay-Doppler detection has yet been made for a comet, radar data have mainly been used to estimate or constrain nucleus parameters from comparisons with other types of observations. For example, comparisons of nucleus radar cross sections with independent size estimates have placed useful bounds on nucleus radar albedos and surface densities.

In addition to the nucleus echo, some comets also show an echo component from large coma grains. This first came as a surprise result from the 1983 observations of C/IRAS-Araki-Alcock (*Campbell et al.,* 1983; *Goldstein et al.,* 1984) and has since been seen for four other comets. The implication is that large-grain emission by comets is common and can account for a significant fraction of the total nucleus mass loss. This is in line with a growing body of evidence from other observations (spacecraft encounters, infrared dust trails, submillimeter continuum, antitails, etc.) that large grains are an important component of the cometary particulate population.

Here we review the various cometary radar findings to date, discuss their implications in the context of other observations, and survey prospects for future work. Although covering much of the same ground as an earlier review article by these same authors (*Harmon et al.,* 1999), the material presented here has been substantially reorganized and updated.

2. RADAR MEASUREMENTS AND DETECTABILITY

All comet radar detections to date have come from Doppler-only observations with the Arecibo S-band (wavelength λ = 12.6 cm), Goldstone S-band (12.9 cm), or Goldstone X-band (3.5 cm) radar systems. Here we summarize the types of measurements made using Doppler-only observations. Discussion of delay-Doppler measurements is deferred to section 5.1.

TABLE 1. Comet radar detections.

Comet	Radar*	Epoch (m/d/y)	Δ (AU)†	References
2P/Encke	A_S	11/2–11/8/1980	0.32	[1,2]
26P/Grigg-Skjellerup	A_S	5/20–6/2/1982	0.33	[2,3]
C/IRAS-Araki-Alcock (1983 H1)	G_S	5/11.94/1983	0.033	[4]
	G_X	5/14.08/1983	0.072	[4]
	A_S	5/11.92/1983	0.033	[5,6]
C/Sugano-Saigusa-Fujikawa (1983 J1)	A_S	6/10–6/12/1983	0.076	[5,7]
1P/Halley	A_S	11/24–12/2/1985	0.63	[8]
C/Hyakutake (1996 B2)	G_X	3/24–3/25/1996	0.10	[9,10]
C/1998 K5 (LINEAR)	A_S	6/14.25/1998	0.196	[11]
C/2001 A2 (LINEAR)	A_S	7/7–7/9/2001	0.26	[12]
C/2002 O6 (SWAN)	A_S	8/8–8/9/2002	0.26	[13]

*A_S = Arecibo S-band (λ = 12.6 cm); G_S = Goldstone S-band (λ = 12.9 cm); G_X = Goldstone X-band (λ = 3.54 cm).

†Distance from Earth at time of observation.

References: [1] *Kamoun et al.* (1982b); [2] *Kamoun* (1983); [3] *Kamoun et al.* (1999); [4] *Goldstein et al.* (1984); [5] *Campbell et al.* (1983); [6] *Harmon et al.* (1989); [7] *Harmon et al.* (1999); [8] *Campbell et al.* (1989); [9] *Ostro et al.* (1996); [10] *Harmon et al.* (1997); [11] *Harmon et al.* (1999); [12] *Nolan et al.* (2001); [13] this paper.

2.1. Doppler Spectrum

A Doppler-only observation involves transmission of an unmodulated (monochromatic) wave and reception of the Doppler-broadened echo. One computes the power spectrum of the received signal, within which a detectable echo would appear as a statistically significant spike or bump sticking up out of the background noise. The echo can appear as a narrow (few Hz wide) spike from the nucleus, or a broad (tens to hundreds of Hz) component from the grain coma. Two comets, C/IRAS-Araki-Alcock and C/Hyakutake, showed echoes from both nucleus and coma. The spectra for these comets are shown in Figs. 1 and 2.

The Doppler spreading of the nucleus spectrum represents the line-of-sight (radial) velocity spread from the apparent rotation of the nucleus. The Doppler frequency for radial velocity V_r and radar wavelength λ is $f = 2V_r/\lambda$. The Doppler bandwidth of a spherical nucleus is then given by

$$B = \frac{8\pi R|\sin\phi|}{\lambda p} = \frac{29.1R(\text{km})|\sin\phi|}{\lambda(\text{cm})p(\text{days})}\ (\text{Hz}) \qquad (1)$$

where R is the nucleus radius, φ is the angle between the apparent rotation axis and the line of sight, and p is the apparent rotation period. For strong detections (e.g., Figs. 3 and 4), bandwidth B is easily determined from the well-

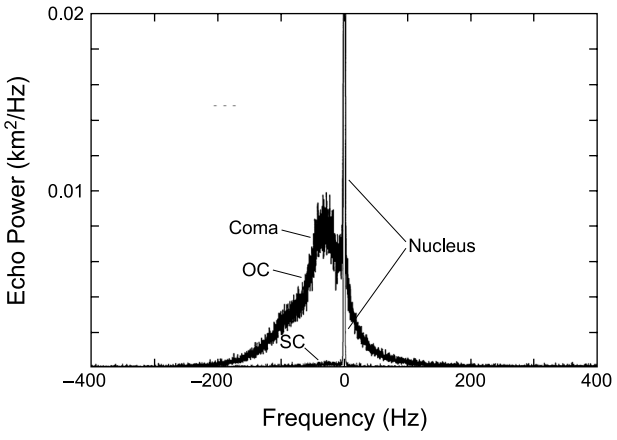

Fig. 1. Doppler spectra (OC and SC polarizations) for C/IRAS-Araki-Alcock showing the narrowband nucleus echo and broadband coma echo. The spectrum is truncated so that only the bottom 2% of the nucleus echo is showing. The spectrum is from Arecibo S-band observations on May 11, 1983 (*Harmon et al.,* 1989).

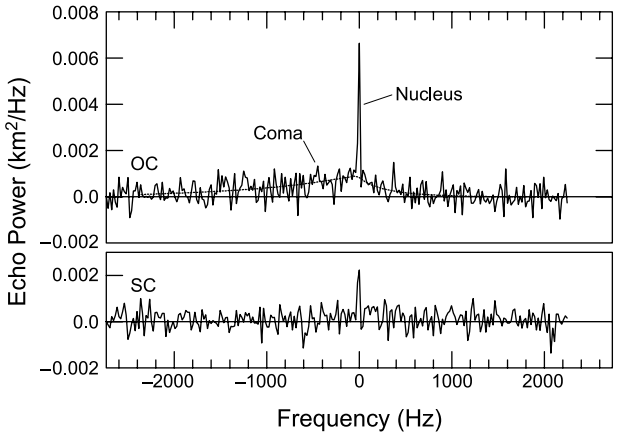

Fig. 2. Doppler spectra (OC and SC polarizations) for C/Hyakutake showing both nucleus and coma echoes. A model fit to the coma echo is also shown (dashed line). The spectrum is from Goldstone X-band observations on March 24, 1996 (*Harmon et al.,* 1997).

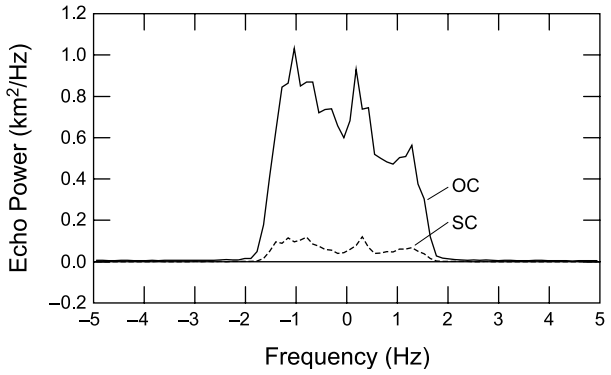

Fig. 3. Doppler spectra (OC and SC polarizations) for the nucleus of C/IRAS-Araki-Alcock, from Arecibo S-band observations on May 11, 1983 (*Harmon et al.,* 1989).

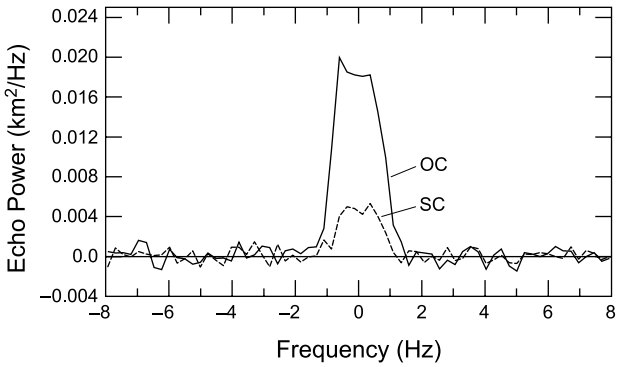

Fig. 4. Doppler spectra (OC and SC polarizations) for the nucleus of C/Sugano-Saigusa-Fujikawa, from Arecibo S-band observations on June 11, 1983 (*Harmon et al.,* 1999).

defined edges of the nucleus spectrum. The shape of the nucleus spectrum is determined by the nucleus shape and orientation as well as by the intrinsic angular scattering law of the surface.

The Doppler spreading of the coma echo represents the collective sum of the radial velocities of all the large grains within the radar beam. The coma spectrum shape is determined by the velocities, sizes, and spatial distribution of the grains, as well as by the cutoff effect of the radar beam.

For the spectra presented here the mean (absolute) Doppler frequency of the nucleus has been subtracted off, so that zero Doppler defines the nucleus center frequency. However, the absolute Doppler offset of the nucleus is of intrinsic interest for refining estimates of a comet's orbital elements. Comet Doppler offsets or refined orbits based on them have appeared in several reports (*Ostro et al.,* 1991b, 1996; *Yeomans et al.,* 1992; *Giorgini,* 2002).

2.2. Radar Cross Section and Albedo

The most fundamental radar parameter measured from the echo is the radar cross section σ. Integrating under the echo Doppler spectrum to get the echo power P_r, σ is then calculated from the radar equation

$$\sigma = \frac{(4\pi)^3 \Delta^4 P_r}{P_t G^2 \lambda^2} \tag{2}$$

where Δ is the comet distance, P_t is the transmitted power, and $G = 4\pi A_e/\lambda^2$ is the beam gain of the radar antenna of effective area A_e. If the size of the nucleus is known or estimated, then σ can be normalized to give a geometric radar albedo

$$\hat{\sigma} = \frac{\sigma}{A_p} \tag{3}$$

where A_p is the apparent projected area of the nucleus. This albedo is useful for estimating surface density (see section 3.2.2).

2.3. Polarization

Echo polarization provides additional information on the target and its scattering properties. All comet radar observations have followed the standard practice of transmitting a circularly polarized wave and receiving in both (orthogonal) senses of circular polarization. These polarization senses on receive are referred to as OC (for "opposite circular"; also called the "polarized" or "expected" sense) and SC (for "same circular"; also called the "depolarized" or "unexpected" sense). Separate echo spectra are computed for each polarization (see Figs. 1–4), from which one can compute OC and SC cross sections σ_{oc} and σ_{sc}. A circular polarization ratio is then defined as $\mu_c = \sigma_{sc}/\sigma_{oc}$.

The OC echo is the stronger of the two ($\mu_c < 1$) for most solar system targets, being the expected sense for specular reflection, while the weaker SC echo is normally attributed to depolarization by wavelength-scale roughness or multiple scattering. For scattering by particle clouds one expects $\mu_c < 1$ when single scattering dominates, with $\mu_c \ll 1$ for particles in the Rayleigh size regime $a < \lambda/2\pi$. When multiple scattering predominates, as for Saturn's rings, one can get $\mu_c \sim 1$.

2.4. Detectability

The strength of the radar detection is given by the detectability D, which is the ratio of the echo power to the rms statistical fluctuation in the noise power. This is given by the radiometer equation $D = (S/N)\sqrt{t\Delta f}$, where S/N is the ratio of the signal and noise spectral densities, t is the integration time, and Δf is the frequency resolution. Combining this with the radar equation (2), and assuming the spectrum is optimally smoothed (matched filtered), gives

$$D = \frac{P_t G^2 \lambda^2 t^{1/2} \eta \sigma}{(4\pi)^3 \Delta^4 k T_s B^{1/2}} \tag{4}$$

where k is Boltzmann's constant, T_s is system temperature, and η is a factor ($\approx$1) that depends on the shape of the echo

TABLE 2. Nucleus echo parameters.

Comet	λ (cm)	σ_{oc} (km^2)	μ_c	B (Hz) [m/s]*
Encke	12.6	1.1 ± 0.7		6 [0.38]
GS	12.6	0.5 ± 0.13	<0.3	<0.5 [<0.03]
IAA	12.6	2.14 ± 0.4	0.105 ± 0.005	3.5 [0.221]
	12.9	2.25†		3.1 [0.20]
	3.5	4.44†	0.25†	20.3 [0.36]
SSF	12.6	0.034 ± 0.008	0.23 ± 0.03	2.5 [0.158]
Hyakutake	3.5	0.13 ± 0.03	0.49 ± 0.10	12 [0.21]
1998 K5	12.6	0.031 ± 0.015	<0.5	<1.5 [<0.09]

*Full (limb-to-limb) Doppler bandwidth in Hz, also expressed as a velocity λB/2 in m/s (in brackets).

†From *Goldstein et al.* (1984), which gives no error estimate.

spectrum. Substituting the current system parameters for the upgraded Arecibo S-band radar in equation (4) and using equation (1) gives

$$D \approx \frac{1.0\sigma(km^2)t^{1/2}(hours)}{\Delta^4(AU)B^{1/2}(Hz)} \geq \frac{2.1\hat{\sigma}R^{3/2}(km)p^{1/2}(days)t^{1/2}(hours)}{\Delta^4(AU)} \quad (5)$$

For the Goldstone X-band radar one substitutes 0.12 for the 2.1 factor. Equation (5) is useful for evaluating future comet radar opportunities (section 5.2).

3. NUCLEUS

Six comets have yielded radar detections of their nuclei (Table 2). The strongest and best-resolved nucleus spectra are those for C/IRAS-Araki-Alcock (henceforth abbreviated IAA) and C/Sugano-Saigusa-Fujikawa (abbreviated SSF), which are shown in Figs. 3 and 4 respectively. Additional nucleus spectra have been published elsewhere, viz. *Kamoun et al.* (1982a,b) (P/Encke); *Goldstein et al.* (1984) (IAA); *Kamoun et al.* (1999) (P/Grigg-Skjellerup); *Harmon et al.* (1997) (C/Hyakutake); *Harmon et al.* (1999) (C/1998 K5).

3.1. Size, Rotation, and Albedo

3.1.1. Size and rotation. The observed nucleus cross sections span two orders of magnitude, from the 2–4 km^2 of IAA down to the 0.03 km^2 of SSF and C/1998 K5. This implies, assuming albedos are equal, that the nucleus sizes vary by about a factor of 10 for the radar-detected sample. This is supported by independent size estimates. *Sekanina* (1988) combined radar data with radio continuum (*Altenhoff et al.,* 1983) and infrared (*Hanner et al.,* 1985) results to deduce that IAA had a large (Halley-size) nucleus measuring 16 × 7 × 7 km and showing an effective radius of 4.4 km at the epoch of the S-band radar observations. Comet SSF, on the other hand, was deduced to be a tiny object (R = 0.37 km) based on its infrared core flux (*Hanner et al.,* 1987). Although there is no independent size estimate for C/1998 K5, its extremely low absolute magnitude (*Marsden,* 1998) suggests that it, too, was very small.

Most size estimates for the three comets with intermediate radar cross sections (Encke, Grigg-Skjellerup, Hyakutake) do, in fact, fall between those of IAA and SSF. For Encke, the infrared results of *Campins* (1988) give R < 2.9 km and the red-visible photometry of *Luu and Jewitt* (1990) gives 2.2 < R < 4.9 km. The most recent size estimate for Encke is the infrared-based value R = 2.4 km of *Fernández et al.* (2000). For Grigg-Skjellerup, *Boehnhardt et al.* (1999) and *Licandro et al.* (2000) give radius estimates of 1.4–1.5 km based on the comet's visual magnitude at large heliocentric distance. Size estimates for Hyakutake vary. The most sensitive radio continuum nondetection gave an upper limit for R of 1.05 km (*Altenhoff et al.,* 1999). Infrared estimates are larger, with R = 2.1–2.4 km (*Sarmecanic et al.,* 1997; *Fernández et al.,* 1996; *Lisse et al.,* 1999).

One can use equation (1) to estimate the rotation period from the Doppler bandwidth B if both R and ϕ are known, or place an upper limit on the period if only R is known. *Sekanina* (1988) showed that the radar bandwidth and coma jet structure of IAA were consistent with a relatively slow rotation period of 2.14 d. For SSF, combining the measured B = 2.5 Hz with R = 0.37 km gives a relatively fast rotation with p < 8.3 h. The estimated bandwidth for Encke (*Kamoun et al.,* 1982b) gives p < 22 h assuming R = 2.4 km. This upper limit encompasses all of Encke's observed periodicities, which span the range 7–22 h (*Samarasinha et al.,* 2004), and includes the recently claimed dominant period of 11 h (*Fernández et al.,* 2002). The estimated Hyakutake bandwidth (*Harmon et al.,* 1997) gives p < 20 h assuming R = 1.2 km, which is consistent with the Hyakutake rotation period estimate of 6.25 h (*Schleicher et al.,* 1998). The Grigg-Skjellerup spectrum was unresolved (*Kamoun et al.,* 1999) and hence yielded no useful constraint on rotation. The echo from 1998 K5 was too weak to readily separate true bandwidth from ephemeris drift, so no rotation constraint is available for that comet. None of the radar-derived rotation period upper limits violate the 3.3-h critical period

TABLE 3. Nucleus radar albedo estimates.

Comet	Albedo*	R (km)	References
Encke	>0.04	<2.9	[1]
	0.02–0.08	2.2–4.9	[2]
	0.06	2.4	[3]
GS	0.08	1.5	[4,5]
IAA†	0.04, 0.07	4.4, 4.9	[6,7]
SSF	0.10	0.37	[8]
Hyakutake	0.01–0.015	2.1–2.4	[9,10,11]
	>0.06	<1.05	[12]

*Total radar cross section divided by πR^2, where R is the tabulated radius. No entry is given for C/1998 K5, for which no radius estimate is available.

†The first and second entries for the albedo and radius correspond to the S-band and X-band observations respectively.

References for radius estimate: [1] *Campins* (1988); [2] *Luu and Jewitt* (1990); [3] *Fernández et al.* (2000); [4] *Boehnhardt et al.* (1999); [5] *Licandro et al.* (2000); [6] *Sekanina* (1988); [7] *Altenhoff et al.* (1983); [8] *Hanner et al.* (1987); [9] *Sarmecanic et al.* (1997); [10] *Fernández et al.* (1996); [11] *Lisse et al.* (1999); [12] *Altenhoff et al.* (1999).

for breakup of a spherical nucleus with 1 g/cm^3 density (*Samarasinha et al.,* 2004).

3.1.2. Albedo. Nucleus radar albedos and the radius values R assumed in their calculation are listed in Table 3. Here we give the total albedo $(\sigma_{oc} + \sigma_{sc})/\pi R^2$, adding an assumed 15% SC component for those comets (Encke and Grigg-Skjellerup) with OC-only detections. The IAA albedo estimates are 0.04 at S-band and 0.07 at X-band, based on the nucleus projected area estimates of *Sekanina* (1988) at the respective epochs of the S-band and X-band observations. The recent radius estimates of 2.4 km for Encke (*Fernández et al.,* 2000) and 1.5 km for Grigg-Skjellerup (*Boehnhardt et al.,* 1999; *Licandro et al.,* 2000) give albedos of 0.06 and 0.08 respectively. The highest $\hat{\sigma}$ is the 0.10 value estimated for SSF from the *Hanner et al.* (1987) infrared size. This high albedo is consistent with the suggestion by Hanner et al. (based on an apparently high thermal inertia and unusually low dust production) that the surface of the SSF nucleus is more highly compacted than normal. For Hyakutake, the R < 1.05 km upper limit from the radio continuum nondetection (*Altenhoff et al.,* 1999) gives $\hat{\sigma} > 0.055$, whereas the larger infrared-based sizes give very low (~0.01) albedos. Such a low radar albedo would imply a very lightly packed nucleus, as suggested by *Schleicher and Osip* (2002). The alternative is that Hyakutake had a "normal" radar albedo similar to those of the other comets, in which case the infrared size estimates must have been biased high. The most likely source of such a bias would be a dust contribution to the infrared flux (*Lisse et al.,* 1999). *Harmon et al.* (1997) estimated the Hyakutake size to be R = 1–1.5 km using IAA's S-band albedo, which they considered to be the most reliable radar albedo available. Clearly, the size and radar albedo of the Hyakutake nucleus remain controversial.

The fact that nucleus radar and optical albedos are low and have about the same values is interesting but probably not significant. While it is true that optical and radar albedo both depend on composition and density, there are important differences. First, optical albedo can be dominated by a thin surface layer, whereas the radar can respond to reflections from meters below the surface. Second, compositional differences are likely to be much more important in the optical than in the radio. For example, a carbonaceous or organic composition could give a surface that is extremely dark optically, but which may not have distinctive radio dielectric properties.

3.2. Surface Properties

3.2.1. Roughness. The resolved nucleus spectra of IAA (Fig. 3) and SSF (Fig. 4) are broad (relative to the total bandwidth B) rather than sharply peaked, which is suggestive of high-angle scattering from very rugged surface relief. The polarization ratios can give some idea of the scale of this relief and its comet-to-comet variation. The relatively low S-band μ_c for IAA is consistent with highly specular scattering from meter-scale or larger structure, although the higher X-band μ_c points to an extra component of smaller rubble. Comet SSF shows a higher S-band μ_c than IAA, indicating roughness that is concentrated more toward decimeter scales. The highest μ_c is the 0.5 measured for Hyakutake at X-band, which suggests a surface that may be nearly saturated with pebble-sized rubble. Hyakutake was an unusually active comet for its size, and its surface texture may be related to that activity. For example, there could be an accumulation of surface debris from ejecta fallback (*Kührt et al.,* 1997). Ice sublimation could also produce surface

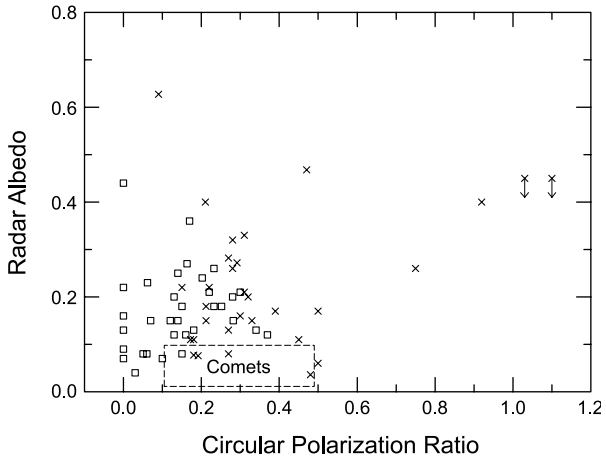

Fig. 5. Distribution of main-belt (squares) and near-Earth (crosses) asteroids in radar albedo and circular polarization ratio (*Benner,* 2002). Also shown for comparison is the range of values for comet nuclei (dashed rectangle).

structure (*Colwell et al.,* 1990). This might explain the roughness for a comet such as SSF, which was very inactive in terms of dust production but very active in the amount of gas it produced for its size.

Comet nucleus polarization ratios (μ_c = 0.1–0.5) are similar to those for many near-Earth and main-belt asteroids (*Ostro et al.,* 2002; *Benner,* 2002; *Magri et al.,* 1999, 2001), as can be seen from the comparison in Fig. 5. This suggests that comets are similar to asteroids in the scale of their surface relief. However, no comets have yet shown the very low depolarization ($\mu_c \sim 0.05$) seen for a few main-belt asteroids or the high depolarization ($\mu_c \sim 1$) seen for a few near-Earth objects.

Comet nuclei also resemble asteroids in their spectral shape. It is customary with asteroids to fit the Doppler spectrum with the function

$$S(f) \propto [1 - (2f/B)^2]^{n/2} \tag{6}$$

which corresponds to the echo spectral shape for a sphere with a scattering law of the form

$$\sigma^o(\theta) \propto \cos^n\theta \tag{7}$$

where $\sigma^o(\theta)$ is the specific cross section as a function of incidence angle θ. Using this model, *Harmon et al.* (1989) found the IAA nucleus followed a uniformly bright (n = 1) or possibly even limb-brightened (n < 1) scattering law based on the sharp edges of its spectrum, arguing that this was evidence for scattering from a chaotic surface with super-wavelength-scale roughness elements giving both specular reflection and shadowing. The SSF spectra more closely followed a Lambert law (n = 2), the cosine-law fits giving n values of 1.4, 2.2, and 2.8 for the three different days. If the scattering is assumed predominantly specular (low μ_c), then the roughness can be estimated from geometric optics (*Mitchell et al.,* 1995). In that case the rms slope θ_r of the surface roughness is related to n by

$$\theta_r = \tan^{-1}\sqrt{2/n} \tag{8}$$

This suggests that comets such as IAA and SSF have rms surface slopes ~50°. This is consistent with the rough topography seen in spacecraft images of Comets Halley and Borrelly (*Weissman et al., 2004*).

3.2.2. Density. If the nucleus surface layer is thick and homogeneous, then one can estimate its bulk density from the radar albedo. If the nucleus radar scattering is predominantly specular, then $\rho_o \approx \hat{\sigma}/g$, where ρ_o is the square of the Fresnel reflection coefficient at normal incidence and g is the backscatter gain. For a $\cos^n\theta$ scattering law in the geometric optics approximation, one has g = (n + 2)/(n + 1). Once ρ_o is estimated, the dielectric constant ε is given by

$$\varepsilon = \frac{(1 + \rho_o^{1/2})^2}{(1 - \rho_o^{1/2})^2} \tag{9}$$

This can then be used to estimate the bulk density d using some suitable expression for $d(\varepsilon)$. In Fig. 6 we plot d as a function of $\hat{\sigma}$ for snow and soil surfaces assuming g = 3/2 (n = 1, assuming geometric optics). Here we have used the expression

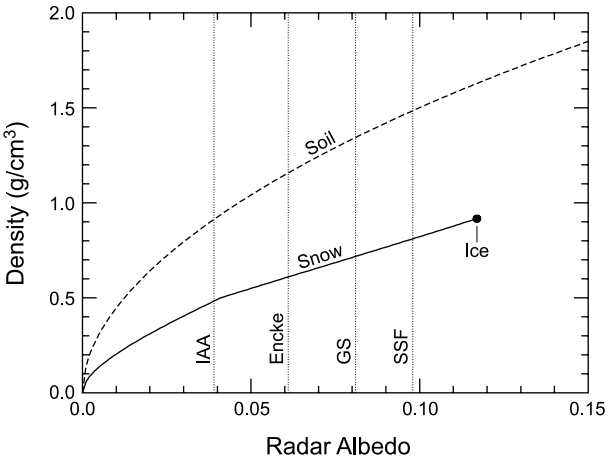

Fig. 6. Bulk density d of the nucleus surface vs. radar albedo $\hat{\sigma}$ for dry snow (solid curve) and a silicate soil (dashed curve). A backscatter gain g = 3/2 was assumed. Various albedo estimates from Table 3 are also shown (vertical dotted lines).

$$d \approx \begin{cases} 0.526(\varepsilon - 1.00) & (\varepsilon \le 1.95) \\ 0.347(\varepsilon - 0.51) & (\varepsilon > 1.95) \end{cases} \tag{10}$$

for the case of dry snow (*Hallikainen et al.,* 1986) and

$$d \approx 3.9\left(\frac{\varepsilon - 1}{\varepsilon + 2}\right) \tag{11}$$

for a soil of silicate powder (*Campbell and Ulrichs,* 1969). From Fig. 6 we see that an IAA-like albedo corresponds to a surface with the consistency of a dense (0.5 g/cm^3) terrestrial snowpack or very fluffy (0.9 g/cm^3) soil. A higher albedo such as that of Comet SSF gives densities closer to that of solid ice or a moderately packed soil. The overall range of albedo estimates indicates that comet nuclei have surface densities in the range 0.5–1.5 g/cm^3. (This density would apply to surface layers down to the penetration depth of the radar wave, which is of the order of 10 wavelengths or so for packed soils.) It is interesting to note that this surface density range is identical to the most recent estimates for the overall bulk density of comet nuclei (*Skorov and Rickman,* 1999; *Ball et al.,* 2001; *Weissman et al.,* 2004), although this does not necessarily imply that nucleus surfaces and interiors have the same structure.

A comparison of albedos indicates that the surfaces of comet nuclei are less dense than asteroid surfaces. Most main-belt asteroids (*Magri et al.,* 1999) and near-Earth asteroids (*Ostro et al.,* 1991a, 2002; *Magri et al.,* 2001; *Benner et al.,* 1997) have higher radar albedos than comets, as can be seen from the comparison in Fig. 5. This al-

bedo difference should translate directly into a difference in reflectivity ρ_o (and density), since the similarity between comet and asteroid scattering implies similar backscatter gains. The near-Earth asteroid 433 Eros is the only asteroid with both a known radar cross section and known mass (and hence known bulk density). Putting the measured total radar albedo of 0.32 of Eros (*Magri et al.,* 2001) into equations (9) and (11) gives a surface density of 3.0 g/cm^3, which is close to the bulk density of 2.7 g/cm^3 estimated from the *NEAR Shoemaker* spacecraft flyby (*Veverka et al.,* 2000) and 3× larger than the comet nucleus bulk densities quoted above; this suggests that the nucleus surface density differences between comets and asteroids inferred from albedo comparisons may reflect differences in total bulk densities for these objects. Another implication of the low comet albedos is that one should expect any extinct comet nuclei masquerading as asteroids to also have low albedos. The asteroids with properties (including low radar albedo) closest to the middle of the domain of comet properties are the 7-km-diameter near-Earth object 1999 JM8 (*Benner et al.,* 2002), for which a cometary origin cannot be excluded (*Bottke et al.,* 2002), and the 0.5-kilometer-diameter object 3757 (1982 XB), which does not have a comet-like orbit.

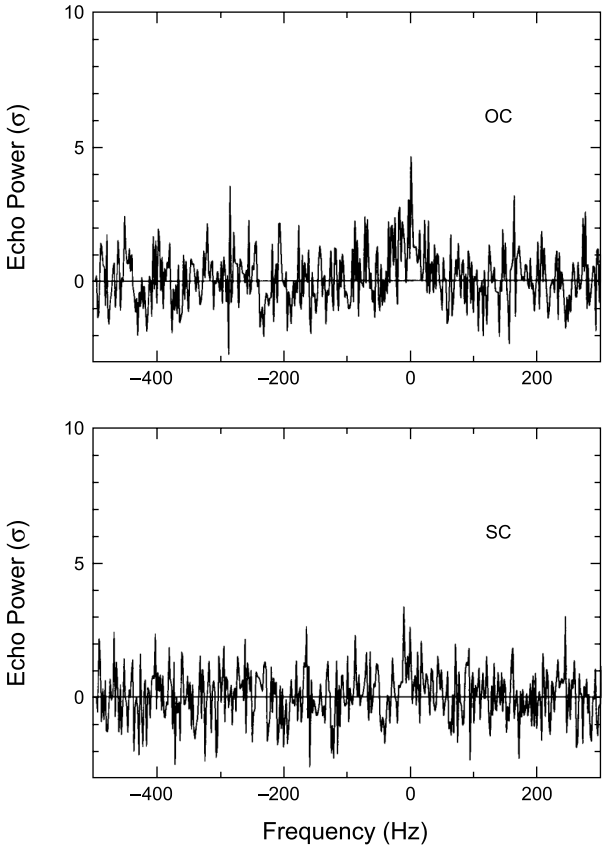

Fig. 7. Doppler spectrum (OC polarization) for P/Halley from a five-day average of Arecibo S-band observations between November 24 and December 2, 1985. The frequency resolution is 1.95 Hz. Smoothing to a resolution of 62 Hz increases the OC detection to nine standard deviations. From *Campbell et al.* (1989).

4. GRAIN COMA

A grain coma echo has been detected from five comets. Two of these, IAA (Fig. 1) and Hyakutake (Fig. 2), gave nucleus detections as well. The three comets giving only coma detections were Halley (Fig. 7), C/2001 A2 (Fig. 8), and C/2002 O6 (Fig. 9). The estimated radar parameters for all the coma detections are listed in Table 4.

One can deduce some basic properties of the large-grain population from rather simple arguments and models, as discussed below.

4.1. Grain Populations and Radar Scattering

Some basic constraints on the large-grain population can be established by simply assuming the grains have a power-law size distribution $n(a) \propto a^{-\alpha}$ with minimum and maxi-

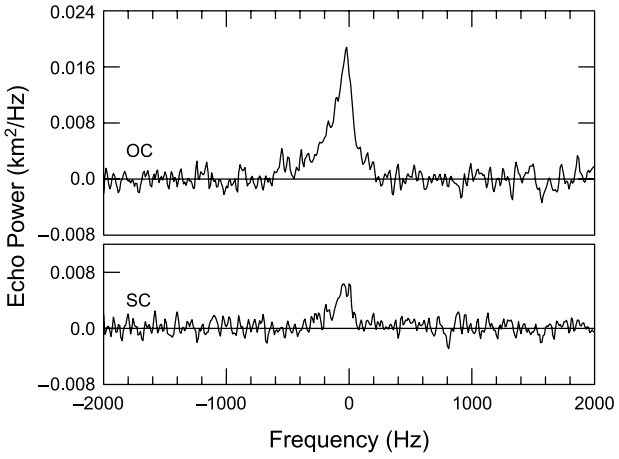

Fig. 8. Doppler spectrum (OC and SC polarizations) for C/2001 A2 (LINEAR) from Arecibo S-band observations on July 7, 2001.

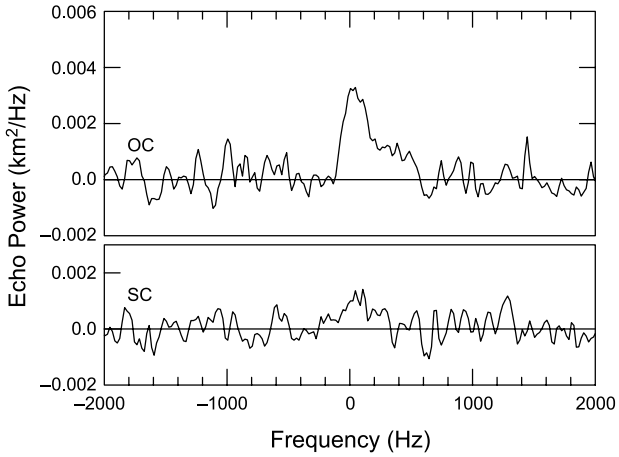

Fig. 9. Doppler spectrum (OC and SC polarizations) for C/2002 O6 (SWAN) from Arecibo S-band observations on August 8 and 9, 2002.

TABLE 4. Grain-coma echo parameters.

Comet	λ (cm)	σ_{oc} (km^2)	μ_c	B_h (Hz) [m/s]*
IAA	12.6	0.80 ± 0.16	0.014 ± 0.003	72 [4.54]
	12.9	0.8†		90 [5.81]
Halley	12.6	32 ± 10	0.52 ± 0.26	42 [2.65]
Hyakutake	3.5	1.33 ± 0.28	0.31 ± 0.12	1180 [20.9]
2001 A2	12.6	4.4 ± 1.3	0.28 ± 0.03	170 [10.7]
2002 O6	12.6	1.1 ± 0.3	0.32 ± 0.08	230 [14.5]

*Full Doppler bandwidth at half-max. in Hz, also expressed as a velocity $\lambda B_h/2$ in m/s (in brackets).
†From *Goldstein et al.* (1984), which gives no error estimate.

mum grain radii of a_o and a_m respectively. The size cutoff a_m not only is useful for assessing the effective size of the radar-scattering grains, but also can have some physical significance. We start with a discussion of the optical depth of the grain coma, which is important for establishing the dominance of single scattering and for determining the radar visibility of the nucleus through the coma (section 4.1.1). We then discuss how a_m is constrained by radar cross section and total grain mass (section 4.1.2) and coma echo polarization (section 4.1.3).

4.1.1. Optical depth. The maximum optical depth to backscatter for a line of sight passing through the center of the grain coma is given by $\tau = \sigma/(4\pi R R_c)$, where σ is the coma radar cross section, R is the nucleus radius, and R_c is the grain coma radius. (Here we assumed that the grain number density in the cloud falls as $1/r^2$ and that $R_c \gg R$.) This result implies that $\tau \sim 10^{-4}$ or less. This can also be used as an upper limit on the ratio of multiple to single scattering. Another useful quantity is the ratio of the absorption and backscatter cross sections, which in the Rayleigh approximation (*Bohren and Huffman,* 1983) is given by

$$\frac{\sigma_a}{\sigma} \approx \left[\frac{(\varepsilon + 2)\varepsilon \tan\delta}{(\varepsilon - 1)^2}\right]\left(\frac{7 - \alpha}{4 - \alpha}\right)\left[1 - \left(\frac{a_o}{a_m}\right)^{4 - \alpha}\right]\left[\frac{a_m}{\lambda/2\pi}\right]^{-3} \quad (12)$$

where ε and $\tan\delta$ are the dielectric constant and loss tangent of the grains respectively. Assuming reasonable grain parameters and setting a_m at the Rayleigh transition ($\lambda/2\pi$) gives $\sigma_a/\sigma \sim 0.1$. (The ratio does not increase for $a_m > \lambda/2\pi$.) Combining this with the backscatter optical depth given above indicates that the absorption optical depth in front of the nucleus is negligible unless a_m is smaller than ~$0.1(\lambda/2\pi)$, which is unlikely from mass and mass-loss arguments (see below). Hence, the nucleus radar detections have probably suffered negligible obscuration by the coma.

4.1.2. Size distribution and total mass. A spherical grain of radius a has a radar cross section of $\pi a^2 Q_b(a)$, where Q_b is the backscatter efficiency. Then, a population of single-scattering grains will have a total radar cross section

$$\sigma = \pi \int_{a_o}^{a_m} n(a) Q_b(a) a^2 da \quad (13)$$

The corresponding total mass of this population is

$$M = \frac{4}{3}\pi d_g \int_{a_o}^{a_m} n(a) a^3 da \quad (14)$$

where d_g is grain density. In the Rayleigh approximation ($a \ll \lambda/2\pi$)

$$Q_b(a) = C_R a^4 \quad (15)$$

where

$$C_R = \left(\frac{2\pi}{\lambda}\right)^4 \left|\frac{\varepsilon - 1}{\varepsilon + 2}\right|^2 \quad (16)$$

Then, from equations (13)–(15), a grain coma with radar cross section σ has a total mass

$$M \approx \sigma \left(\frac{4 d_g}{3 C_R}\right)\left(\frac{7 - \alpha}{4 - \alpha}\right)\left[1 - \left(\frac{a_o}{a_m}\right)^{4 - \alpha}\right] a_m^{-3} \quad (17)$$

This a_m^{-3} dependence shows the extreme sensitivity of the mass M to maximum grain size in the Rayleigh regime, a result of the rapidly decreasing Rayleigh backscatter efficiency with smaller grain size. Using this equation, *Harmon et al.* (1989) and *Campbell et al.* (1989) showed that making $a_m < 0.5$ mm resulted in a total mass in grains exceeding the nucleus mass for both IAA and Halley, from which they concluded that the effective grain size must have been at least a few millimeters.

4.1.3. Polarization and maximum grain size. The coma echo from Comet IAA was only ~1% depolarized (μ_c = 0.014), which is the smallest depolarization ever measured for a solar system radar echo. This is consistent with a physically real cutoff a_m not much larger than $\lambda/2\pi$. [It is shown in *Harmon et al.* (1989) that μ_c for irregular grains increases dramatically from ~10^{-2} or less to >0.1 as radius approaches $\lambda/2\pi$, although the transition size can be larger for low-density grains.] Combining this with the lower bounds on a_m from the total mass (section 4.1.2) and mass-loss rate (section 4.2.3) points to a sharp size cutoff at a few centimeters. As pointed out by *Harmon et al.* (1989), this would be consistent with the gravitational cutoff in simple gas-drag theories of particle ejection (section 4.2.1). However, since this apparent cutoff is close to the Rayleigh polarization threshhold, one would expect to see coma echoes from other comets with μ_c much higher than for IAA, owing to a less massive nucleus or more explosive activity. Although both Halley and Hyakutake showed hints of nonnegligible coma depolarization, the only firm detection of significant coma depolarization is from the recent detection of C/2001 A2

(*Nolan et al.,* 2001). Since the nucleus of this comet had split prior to the radar observations (*Sekanina et al.,* 2002), it is possible that the depolarization was from boulder-sized debris left over from the splitting or produced in violent activity of small, freshly exposed subnuclei.

4.2. Grain Ejection and Echo Modeling

Further analysis of the coma echo requires modeling the grain ejection process and estimating the mass-loss rates required to sustain the observed grain coma. A good starting point is to assume that the grain emission process is a continuous one in which grains are ejected as free (unbound) particles in the comet orbit frame. That the grains are predominantly unbound is consistent with the lack of a clear symmetric component about the nucleus echo in the coma spectra for IAA and Hyakutake (Figs. 1 and 2). While it is expected that some grains will be injected into circumnuclear orbits (*Richter and Keller,* 1995; *Fulle,* 1997), Fulle estimates that only about 1% of the ejected grains will do so; this would not be enough to accumulate a significant bound population, especially if the grains are undergoing evaporation or disintegration.

4.2.1. Gas drag models. For grain ejection we adopt the canonical model first formulated by *Whipple* (1951) and refined by others. Assuming a uniform radial outflow of gas with thermal expansion velocity V_g, one can write a differential equation for the outward drag velocity V of the grains (*Wallis,* 1982; *Gombosi et al.,* 1986)

$$M_g V \frac{dV}{dr} = \frac{1}{2} C_D \pi a^2 (V_g - V)^2 \frac{ZR^2}{V_g r^2} - \frac{GM_g M_n}{r^2} \quad (18)$$

where C_D is the drag coefficient, Z is the surface gas mass flux, R is nucleus radius, G is the gravitational constant, and M_g and M_n are grain and nucleus mass respectively. Then, assuming that the grain and nucleus are spheres of density d_g and d_n, that V_g is constant with radial distance r, and that $V \ll V_g$, integrating equation (18) gives a terminal grain velocity

$$V_t(a) = C_v a^{-1/2} (1 - a/a_m)^{1/2} \quad (19)$$

where

$$C_v = \left(\frac{3 C_D V_g Z R}{4 d_g} \right)^{1/2} \quad (20)$$

is a velocity scale factor, and

$$a_m = \frac{9 C_D V_g Z}{32 \pi G R d_n d_g} \quad (21)$$

is a maximum grain size in the gravitational correction factor $(1 - a/a_m)^{1/2}$. [Equations (20) and (21) are equivalent to equation (4) of *Jewitt and Matthews* (1999) and equation (72) of *Gombosi et al.* (1986) respectively.] One has $C_D = 2$ for a solid sphere, although the drag coefficient can be higher for fluffy grains (*Keller and Markiewicz,* 1991). The velocity V_g is often taken to be the thermal expansion velocity at the surface multiplied by some correction factor to allow for expansion effects; this factor is ≈9/4 in *Finson and Probstein* (1968). Nonradial or asymmetric expansion can also give V_t different from the canonical model (*Crifo,* 1995).

Using these equations, *Harmon et al.* (1989) argued that the IAA coma echo was consistent with the simple gas drag model. Taking a_m = 3 cm as a reasonable cutoff size (based on the mass and polarization arguments above) requires a gas flux Z of ~1×10^{-5} g/cm² s, a reasonable value when compared with the 5×10^{-5} g/cm² s sublimation rate for clean ice at 1 AU. This also gives reasonable grain velocities (8 m/s for a = 1 cm) and a good match to the Doppler spread in the coma spectrum model (see next section). Hyakutake did not fit so neatly into this picture, its much broader spectrum requiring higher grain velocities (40 m/s for a = 1 cm) than for IAA despite its smaller nucleus (*Harmon et al.,* 1997). This implied a much higher effective gas flux (~4×10^{-4} g/cm² s), or much fluffier grains, or both. Since Hyakutake's nominal surface active fraction is about 1.0 assuming Z = 5×10^{-5} g/cm² s, then the effective Z must have been much higher than this in the discrete active regions that were observed to dominate the emission (*Schleicher et al.,* 1998). Grain fluffiness could also boost the ejection velocity by lowering grain density and raising the drag coefficient.

4.2.2. Doppler spectrum modeling. The shape of the Doppler spectrum contains information on the grain velocity vectors and spatial distribution. Although the grain coma cannot be uniquely characterized from its spectrum, some useful results have been obtained by treating the forward problem of comparing the observed spectrum with model spectra computed from trial input parameters. If one starts with the gas-drag model (section 4.2.1) and ignores radiation pressure, then it is fairly straightforward to compute a Doppler spectrum by assuming a production size distribution and summing over discrete grain emission times and directions (*Harmon et al.,* 1989). Once the nucleus and grain properties are assumed, then the remaining free parameters in the model are the ejection geometry and Z (or a_m).

Model spectra have been computed for the coma echoes from IAA (*Harmon et al.,* 1989) and Hyakutake (*Harmon et al.,* 1997). The shape and offset of the IAA coma spectrum could be well modeled (Fig. 10) by invoking a sunward grain emission fan with centroid aimed below the comet orbit plane in a direction consistent with the orientation of the infrared and visual dust fans. No doubt this was aided by the fact that IAA was a slow rotator with an unusually stable sunward fan (*Sekanina,* 1988). The model shown in Fig. 10 has Z = 1.2×10^{-5} g/cm² s and a_m = 3 cm, which is consistent with the observed echo polarization and gives plausible nucleus mass-loss rates and gas fluxes. A model spectrum for Hyakutake is shown overplotted in Fig. 2. Here a much higher Z of 4×10^{-4} g/cm² s [V_t (1 cm) = 40 m/s] was required to reproduce the large Doppler spread (see discussion in previous section). Since the

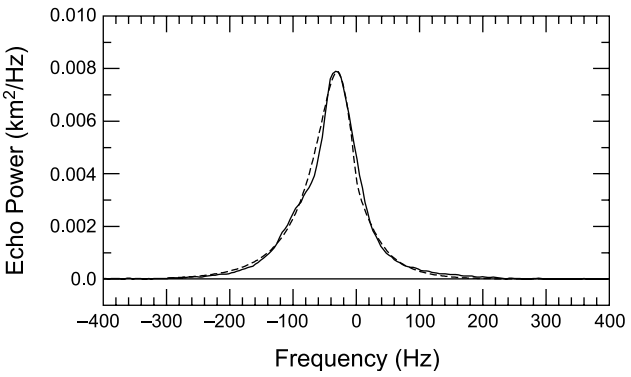

Fig. 10. Model coma spectrum (dashed line) overplotted on the OC coma echo for C/IRAS-Araki-Alcock. The data spectrum (solid line) has been smoothed to 10-Hz resolution. See text for details.

dust emission for this fast rotator was more complicated than for IAA, no attempt was made to arrive at a single consistent model for the grain emission geometry.

4.2.3. Mass-loss rates. If one assumes that the grain coma is replenished by continuous particle ejection, then the coma radar cross section can be used to estimate the mass-loss rate in large grains. We assume the grains have a production-rate size distribution $\dot{n}(a) \propto a^{-\alpha}$. The mass-loss rate $\dot{M}$ is given by

$$\dot{M} = \frac{4}{3}\pi d_g \int_{a_o}^{a_m} \dot{n}(a) a^3 da \tag{22}$$

The total radar cross section of the grains in the radar beam is

$$\sigma = \pi \int_{a_o}^{a_m} \dot{n}(a) L(a) Q_b(a) a^2 da \tag{23}$$

where L(a) is the mean lifetime of a grain of radius a within the beam. If the grains are ejected isotropically and remain intact as they traverse the beam, then the mean lifetime is the mean beam transit time $\pi h/2V_t(a)$, where h is the half-width of the cylinder defined by the radar beam at the comet. Then, combining equations (19)–(23) gives

$$\dot{M}(a_m) = \sigma \left(\frac{8Rd_g}{3}\right)\left(\frac{8}{3}\pi G d_n\right)^{1/2} \left[1 - \left(\frac{a_o}{a_m}\right)^{4-\alpha}\right] a_m^{9/2-\alpha} [(4-\alpha)\pi h I]^{-1} \tag{24}$$

where

$$I = \int_{a_o}^{a_m} \frac{a^{5/2-\alpha} Q_b(a)}{(1 - a/a_m)^{1/2}} da \tag{25}$$

This is the same as equation (B9) of *Harmon et al.* (1989). [An incorrectly rewritten version of this equation appeared as equation (14) of *Harmon et al.* (1999), although the calculations in that paper were based on the correct original equation.] For $a < \lambda/2\pi$ one gets a Rayleigh approximation for $\dot{M}$ by using the following analytic solution for the integral

$$I = C_R B(1/2, 15/2 - \alpha) a_m^{15/2-\alpha} \tag{26}$$

where B is the beta function. Implicit in equation (24) is the assumption that the velocity scale factor C_v is a function of a_m. If, on the other hand, one has an independent estimate of C_v (say, from the width of the Doppler spectrum), then one could treat it (and a_m) as a constant, to give the modified expression

$$\dot{M}(a_{max}) = \sigma \left(\frac{8C_v d_g}{3}\right)\left[1 - \left(\frac{a_o}{a_{max}}\right)^{4-\alpha}\right] a_{max}^{4-\alpha} [(4-\alpha)\pi h I]^{-1} \tag{27}$$

where a_{max} ($<a_m$) can be taken as some other (nongravitational) cutoff size that replaces a_m as the upper integration limit in equation (25).

In Fig. 11 we show results of mass-loss rate calculations for three comets. Here we have used equation (24) to calculate $\dot{M}(a_m)$ for IAA and Halley, and equation (27) to calculate $\dot{M}(a_{max})$ for Hyakutake [assuming V_t (1 cm) = 40 m/s]. Mie theory was used to calculate Q_b assuming the grains to be spherical snowballs with density d_g = 0.5 g/cm³ (refractive index = 1.4). We took the production rate size distribution to be an $\dot{n}(a) \propto a^{-3.5}$ power law between a_o = 1 μm and the cutoff size. The α = 3.5 power law was chosen not only because it conforms to size distributions measured for Halley (*McDonnell et al.,* 1986) and Hyakutake (*Fulle et al.,* 1997), but also because it has the convenient property of giving an $\dot{M}$ that is determined primarily by the larger (radar-reflecting) grains and that is relatively insensitive to the precise value of α. The Rayleigh regime ($a_m < \lambda/2\pi$) in Fig. 11 shows the $\dot{M}(a_m) \propto a_m^{-3}$ behavior expected from substitution of equation (26) in equation (24). It is this strong Rayleigh size dependence that requires the presence of large (greater than millimeter-sized) grains in order to explain the radar cross sections for reasonable mass-loss rates; for example, taking a_m = 1 mm implies an $\dot{M}$ that would have a typical comet nucleus losing most of its mass during a single perihelion passage. The $\dot{M}$ curves flatten out at the larger sizes ($a_m > \lambda/2\pi$), corresponding to large-grain production rates in the range 3×10^5–1×10^6 g/s.

4.2.4. Comparisons with other mass-loss rate estimates. By comparing the radar-derived production rates with other measurements sensitive to smaller dust particles, we can get some idea of the relative importance of the large grains to the overall particulate population of the coma. Infrared measurements for IAA (*Hanner et al.,* 1985) gave dust production rates of 1–2 × 10^5 g/s. This is a bit smaller than the rates shown in Fig. 11 and would be consistent with an overall production size distribution spectral index α = 3.8. Clearly, large grains contributed a substantial fraction of the

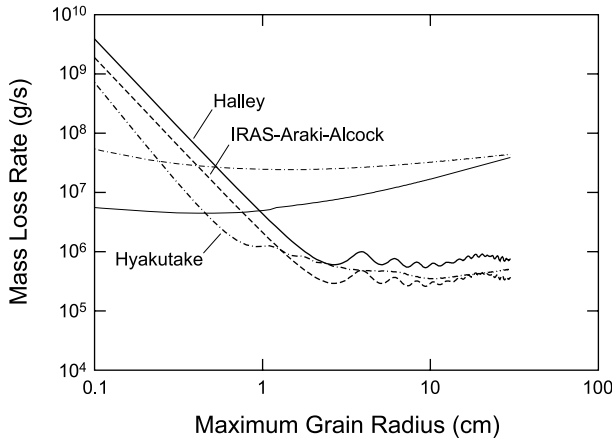

Fig. 11. Mass-loss rate $\dot{M}$ vs. maximum grain radius a_m for Comets Halley (solid), IRAS-Araki-Alcock (dashed), and Hyakutake (dot-dashed). These were computed using the measured radar cross sections and assuming the grains to be 0.5 g/cm^3 snowballs with an $a^{-3.5}$ production size distribution. Also shown are $\dot{M}$ curves computed on the basis of the measured radio continuum fluxes for Halley and Hyakutake (lighter curves).

mass loss for IAA. Comparison of the Halley curve in Fig. 11 with the dust production rate of 2×10^6 g/s from infrared measurements indicates large grains constituted a slightly smaller fraction of the mass loss for this comet, although *Giotto* dust detector results (*McDonnell et al.,* 1986) suggest that Halley's large-grain production should have dominated the mass loss with $\dot{M} = 5 \times 10^6$ g/s at the time of the Arecibo observations. The dust production rate of 5×10^6 g/s estimated for Hyakutake (*Fulle et al.,* 1997) exceeds by several times the radar-derived rate for $a_m >$ 1 cm (Fig. 11), suggesting that large grains were important but not dominant for this comet.

Since the radar-derived mass-loss rates assume that the grains remain intact as they traverse the radar beam, the $\dot{M}$ curves in Fig. 11 are actually lower limits and hence may underestimate the relative contribution of large grains to the total particulate mass loss. Grain evaporation and disintegration are, in fact, believed to be important processes (*Hanner,* 1981; *Combi,* 1994). It has been estimated that (at 1 AU) ejected dirty-ice grains with radii of 1 mm and 1 cm only travel 100 km and 2000 km respectively before evaporating (*Hanner,* 1981; *Harris et al.,* 1997). This may explain why the Arecibo and Goldstone S-band coma echoes for IAA gave the same radar cross section despite the fact that the Goldstone beam was 3× wider than the 2200 km subtended by the Arecibo beam at the comet, although icy grains from IAA were not detected in the infrared observations of *Hanner et al.* (1985). For Halley, *Campbell et al.* (1989) also suggested that ignoring grain evaporation might account for the apparent discrepancy between the radar and *Giotto* grain production rates. Similarly, many of the large grains from Hyakutake may have evaporated or disintegrated before traversing a substantial fraction of the 7000-km Goldstone beam. This is supported by the photometric data of *Schleicher and Osip* (2002), which show a slow falloff in CN, C_2, and dust with increasing aperture size that is consistent with fragmentation or evaporation of grains from that comet. Further support comes from *Harris et al.* (1997), who argued that evaporation of large icy grains produced Hyakutake's spherical gas coma and accounted for 23% of the comet's total gas production. This would give 1×10^6 g/s in secondary gas from grains, so the total large-grain mass lost to disintegration could have been significantly higher than this if the volatile fraction was low. It is clear that the total mass contained in large grains is high enough that grain fragmentation could be an important secondary source of coma gas in the typical active comet.

Finally, it is worthwhile comparing the radar $\dot{M}$ values with those estimated from millimeter-wave continuum observations, which are also sensitive to large grains (*Jewitt and Luu,* 1992). An equivalent continuum equation for $\dot{M}$ can be written by replacing σ in equations (24) or (27) with $S\lambda^2\Delta^2/2kT$ and replacing Q_b in equation (25) with Q_a, where S is the continuum flux density, T is grain temperature, and Q_a is the grain absorption efficiency. This has been used to compute $\dot{M}$ curves (Fig. 11) from the 3.5-mm continuum detection of Halley (*Altenhoff et al.,* 1986) and the 1.1-mm continuum detection of Hyakutake (*Jewitt and Matthews,* 1997). [We have not included a curve for IAA, as the 1.3-cm continuum detection by *Altenhoff et al.* (1983) appears to have been dominated by thermal emission from the nucleus, as was also argued by *Harmon et al.* (1989).] Note that these curves do not show the same extreme sensitivity to a_m in the Rayleigh regime as the radar curves, which reflects the different behaviors of Q_a and Q_b. The comparison with radar is uncertain because of the sensitivity of the continuum curves to assumed grain properties such as porosity and electrical conductivity, although the sensitivity to the assumed conductivity becomes less important as the larger grains become optically thick. For the curves in Fig. 11 we assume the grains to be dirty snowballs with 0.5 g/cm^3 density and 0.01 imaginary part refractive index. The radar beam was 4× and 6× larger than the continuum beam for Halley and Hyakutake respectively, so any grain evaporation would also affect the comparison. Note that the continuum curves are significantly higher than the radar curves for a_m larger than 1 cm. Including grain evaporation would reduce some of this discrepancy. A possible way to remove the remaining discrepancy is to invoke fluffier grains (which would also help to explain the high grain velocities inferred from the Hyakutake coma spectrum, as mentioned in section 4.2.1). This is because increasing the grain porosity raises the absorption per unit mass (or opacity κ) as it lowers the backscatter per unit mass, the combined effect being to bring the radio and radar curves closer together (*Harmon et al.,* 1997). This implies that κ(1 mm) would have to be higher than the κ(1 mm) = 2–3 cm^2/g that characterizes the curves in Fig. 11. In fact, *Altenhoff et al.* (1999) assumed "fluffy dust" with κ(1 mm) = 75 cm^2/g to estimate Hyakutake's dust production from their

radio continuum observations. This accounted for the very large discrepancy that they noted between their production rates and those inferred by *Jewitt and Matthews* (1997) using a much lower $\kappa(1\ \mathrm{mm}) = 0.5\ \mathrm{cm^2/g}$ value typical of interstellar dust.

5. FUTURE WORK

5.1. Radar Imaging: Delay-Doppler and Interferometric

The highest priority of future cometary radar is to obtain images of the nucleus and/or coma echoes. Imaging could provide data on nucleus size, shape, rotation, and surface features, as well as the size of the grain coma and its position relative to the nucleus. It can also be used to more accurately determine the nucleus albedo and scattering law. Imaging can be done using either the delay-Doppler method or an interferometer.

Delay-Doppler combines pulsed or coded transmission with spectral analysis in order to resolve the echo into cells in delay-Doppler space. The detectability in a given delay-Doppler cell is roughly given by $D/(N_d\sqrt{N_D})$, where D is the Doppler-only detectability from equation (4) and N_d and N_D are the number of delay and Doppler bins, respectively, across the target. Any comet nucleus passing within about 0.1 AU should provide a good delay-Doppler imaging opportunity for Arecibo (*Harmon et al.,* 1999), although crude imaging or delay-profiling suitable for size estimation may be feasible at larger distances. A delay-Doppler image could provide direct information on a nucleus and also be used to construct a three-dimensional model of the rotating object, in a similar manner to work done on near-Earth asteroids (*Ostro et al.,* 1995; *Hudson and Ostro,* 1995). If the radar images have adequate orientational coverage and an adequate time span, then the modeling can decipher the nucleus spin state. This would be of particular interest for slow rotators because of their tendency for non-principle-axis rotation (*Ostro et al.,* 2001; *Samarasinha and A'Hearn,* 1991; *Hudson and Ostro,* 1995; *Samarasinha et al.,* 2004). Also, any absolute range measurement would provide even more accurate orbit astrometry than could be derived from Doppler alone. For the grain-coma echo, the extra information provided by a delay-resolved echo would remove some of the ambiguity encountered in coma-echo modeling using Doppler spectra alone. However, coma delay-Doppler images would pose their own special interpretation problems, as the mapping problem is unlike that for a rigid rotating body. Furthermore, unlike the nucleus echo, a coma echo is likely to be "overspread" (product of delay depth and Doppler bandwidth >1), which would require a special observing strategy as discussed by *Harmon* (2002).

Interferometric imaging offers an alternative to delay-Doppler imaging. The Very Large Array (VLA) can potentially image coma echoes from Goldstone 3.5-cm transmissions with a synthesized beam as small as 0.24 arcsec. This bistatic method, which has been applied successfully to a few asteroids as well as Mercury, Venus, Mars, and Saturn's rings, has significant potential for direct plane-of-sky imaging of the grain comae of close-approaching comets (*de Pater et al.,* 1994). The VLA resolution is too coarse for nucleus imaging, but bistatic radar observations with the Very Long Baseline Array (VLBA) would be suitable, with resolutions at S- and X-bands of 3 mas and 0.8 mas respectively.

5.2. Short-Period Comet Opportunities

Radar observations in the coming years will include a mix of short-period and new comets. The short-period comets include the ecliptic comets (and their Jupiter-family subset), with a putative Kuiper belt origin, and the Halley-type comets, most of which probably come from the Oort cloud (*Levison,* 1997). The "new" comets include both dynamically new objects and newly discovered long-period comets. Although new comets such as IAA may well offer the best radar opportunities, the short-period comets hold some intrinsic interest. They are the most likely targets for spacecraft missions, for which groundbased radar can provide both mission support and a complementary dataset. Also, though relatively inactive compared to some new comets, they are thought to play an important role in the interplanetary dust budget and are the source of meteor streams and infrared dust trails; hence, echoes from their large-grain comae are of interest. There are several good short-period comet radar opportunities over the next decade or so. These are listed in Table 5. Below we discuss some of the more interesting apparitions. (We include the Encke apparition of 2003 in this discussion and Table 5, even though the observations planned for that apparition will have been done by the time this book goes to press.) The quoted detectabilities are computed from equation (5) assuming a 1-h integration time, a nucleus albedo of 0.05, and (unless otherwise noted) a rotation period of 0.5 d. The D values also assume $|\sin\phi| = 1$, and therefore represent lower limits.

5.2.1. 2P/Encke. Although one of the most intensely studied of all comets, Encke's nucleus properties remain uncertain. Observations in 2003 should give D ~ 60 at Arecibo and ~3 at Goldstone. This may allow some crude delay-Doppler imaging and a direct size estimate. While not a very active comet, Encke is known to produce centimeter-sized grains and to be the source of the Taurid meteors and an infrared dust trail (*Epifani et al.,* 2001; *Reach et al.,* 2000). The large grains may give a weak coma detection.

5.2.2. 73P/Schwassmann-Wachmann 3. This comet makes a very close pass in 2006 and offers a nominally excellent, if unpredictable, radar opportunity. This comet split into three main pieces during its 1995 apparition, those pieces reappearing at the 2001 apparition. If each piece has one-third the mass of a R = 1 km parent body (*Boehnhardt et al.,* 1999), its detectability should be ~1000 at Arecibo (~60 at Goldstone), making this a good imaging opportunity. Detectable coma echoes are also likely.

5.2.3. 8P/Tuttle. This little-studied object is the only Halley-type comet in this sample and thus the only one likely to have an Oort cloud origin. The only known radius estimate is R = 7.3 km from optical magnitude measure-

TABLE 5. Future radar opportunities for short-period comets (passing within 0.5 AU through year 2020).

Comet	Date (m/d/y)*	Δ (AU)†
2P/Encke	11/17/2003	0.261
73P/Schwassmann-Wachmann 3	5/12/2006	0.051–0.076‡
8P/Tuttle	1/2/2008	0.252
6P/d'Arrest	8/10/2008	0.353 [0.375]
103P/Hartley 2	10/21/2010	0.120
45P/Honda-Mrkos-Pajdušáková	8/15/2011	0.060§ [0.220]
2P/Encke	10/17/2013	0.478
P/2000 G1 (LINEAR)	3/22/2016	0.032 [0.105]
45P/Honda-Mrkos-Pajdušáková	2/11/2017	0.087
41P/Tuttle-Giacobini-Kresak	3/27/2017	0.136 [0.190]
21P/Giacobini-Zinner	9/11/2018	0.380
64P/Swift-Gehrels	10/28/2018	0.444
46P/Wirtanen	12/16/2018	0.075

*Date of closest approach.
†Distance from Earth at closest approach (with closest distance for Arecibo observations, if different, in brackets).
‡Range of distances for fragments B, C, and E.
§Just below Goldstone horizon at this distance.

ments by *Licandro et al.* (2000) at large heliocentric distances. This would place it in the Halley size class, so a radar-based size estimate would be of considerable interest. If Tuttle is really this large, it would give D ~ 300 at Arecibo (~17 at Goldstone). This comet is the parent of the Ursid meteor stream (*Jenniskens et al.,* 2002), so there is the potential for a coma echo.

5.2.4. 6P/d'Arrest. This second 2008 apparition is less favorable than that of Tuttle, owing to the larger Δ and southerly declinations. Using R = 2.7 km (*Lisse et al.,* 1999) and the oft-quoted short rotation period of 5.2 h (itself of intrinsic interest) gives D ~ 5 for Arecibo. This comet shows an antitail (*Fulle,* 1990) and must therefore produce some large grains.

5.2.5. 103P/Hartley 2. The small Δ of this comet in 2010 offers a good radar opportunity despite its apparent small size. Using R = 0.56 km (*Jorda et al.,* 2000) gives a D ~ 150 at Arecibo and ~9 at Goldstone. This comet is fairly active for its size and a likely producer of large grains (*Epifani et al.,* 2001), so a coma echo is possible.

5.2.6. 45P/Honda-Mrkos-Pajdušáková. In 2011 this comet does not enter the Arecibo declination window until well past close approach, making it a better target for Goldstone. Assuming R = 0.34 (*Lamy et al.,* 1999), the Goldstone detectability is about 20 by the time the comet reaches a reasonable sky elevation (Δ = 0.08 AU). The Arecibo D for the 2017 apparition is 250. Although a dust-poor comet, it is known to be the source of the Alpha Capricornid meteors, so a coma echo is possible.

5.2.7. 46P/Wirtanen and other mission targets. The Jupiter-family comet Wirtanen is of special interest as the target of the ROSETTA spacecraft rendezvous in 2011. Unfortunately, this comet only comes within 0.92 AU at its 2008 apparition, making it an impossible target given its estimated size of R = 0.6 km (*Lamy et al.,* 1998; *Boehnhardt et al.,* 2002). There is a nominally excellent opportunity in 2018, although the comet's large nongravitational acceleration (*Jorda and Rickman,* 1995) makes the distance prediction uncertain. Comet 9P/Tempel 1, the target of the Deep Impact mission, approaches within 0.71 AU in early May 2005, two months before the spacecraft encounter. Taking R = 3 km (*Lamy et al.,* 2001) and p = 41 h (*Meech et al.,* 2002) gives an Arecibo detectability of only D = 3. Still, an Arecibo attempt at a nucleus detection at closest approach is probably warranted. An attempt might also be made to look for echoes from debris ejected in the July 4, 2005, impact experiment, although Tempel 1 will be even more distant (0.89 AU) at that time. Finally, the Stardust mission target, 81P/Wild 2, is not observable from Arecibo at less than 1.5 AU for the next two decades.

6. SUMMARY

Earth-based radar has proven to be an important tool for studying close-approaching comets. The various nucleus detections show comet nuclei to be rough objects with relatively low surface densities. They have also established a factor-of-10 nucleus size range for this limited sample, based on the observed range of radar cross sections. A large fraction of the radar-detected comets have been found to show broadband echoes from large coma grains. This has provided some of the strongest evidence yet for the prevalence of large-grain emission by comets. With radar-derived productions rates ~10^6 g/s, large (approximately centimeter-sized) grains must constitute a significant fraction of the total mass loss for some comets.

The full potential of cometary radar will not be realized until radar imaging of a comet is achieved. Delay-Doppler imaging holds the potential for accurately determining nucleus properties such as size, shape, spin state, albedo, and scattering law. An imaged or delay-resolved coma echo would also be of considerable interest. A few of the upcoming short-period comet apparitions may afford opportunities for at least crude nucleus imaging. Favorable imaging opportunities from new-comet apparitions are also anticipated.

REFERENCES

Altenhoff W. J., Batrla W., Huchtmeier W. K., Schmidt J., Stumpff P., and Walmsley M. (1983) Radio observations of Comet 1983d. *Astron. Astrophys., 125,* L19–L22.

Altenhoff W. J., Huchtmeier W. K., Schmidt J., Schraml J. B., Stumpff P., and Thum C. (1986) Radio continuum observations of comet Halley. *Astron. Astrophys., 164,* 227–230.

Altenhoff W. J. and 20 colleagues (1999) Coordinated radio continuum observations of comets Hyakutake and Hale-Bopp from 22 to 860 GHz. *Astron. Astrophys., 348,* 1020–1034.

Ball A. J., Gadomski S., Banaszkiewicz M., Spohn T., Ahrens T. J., Whyndham M., and Zarnecki J. C. (2001) An instrument for in situ comet nucleus surface density profile measurement by gamma ray attenuation. *Planet. Space Sci., 49,* 961–976.

Benner L. A. M. (2002) Summaries of asteroid radar properties [online]. California Institute of Technology, Pasadena [cited Oct. 1, 2002]. Available on line at http://echo.jpl.nasa.gov/

~lance/asteroid_radar_properties.html.

Benner L. A. M. and 12 colleagues (1997) Radar detection of near-Earth asteroids 2062 Aten, 2101 Adonis, 3103 Eger, 4544 Xanthus, and 1992 QN. *Icarus, 130,* 296–312.

Benner L. A. M., Ostro S. J., Nolan M. C., Margot J.-L., Giorgini J. D., Hudson R. S., Jurgens R. F., Slade M. S., Howell E. S., Campbell D. B., and Yeomans D. K. (2002) Radar observations of asteroid 1999 JM8. *Meteoritics & Planet. Sci., 37,* 779–792.

Boehnhardt H., Rainer N., and Schwehm G. (1999) The nuclei of comets 26P/Grigg-Skjellerup and 73P/Schwassmann-Wachmann 3. *Astron. Astrophys., 341,* 912–917.

Boehnhardt H., Delahodde C., Sekiguchi T., Tozzi G. P., Amestica R., Hainaut O., Spyromilio J., Tarenghi M., West R. M., Schulz R., and Schwehm G. (2002) VLT observations of comet 46P/Wirtanen. *Astron. Astrophys., 387,* 1107–1113.

Bohren C. F. and Huffman D. R. (1983) *Absorption and Scattering of Light by Small Particles*. Wiley & Sons, New York. 530 pp.

Bottke W. F., Morbidelli A., Jedicke R., Petit J.-M., Levison H. F., Michel P., and Metcalfe T. S. (2002) Debiased orbital and absolute magnitude distribution of the near-Earth objects. *Icarus, 156,* 399–433.

Campbell D. B., Harmon J. K., Hine A. A., Shapiro I. I., Marsden B. G., and Pettengill G. H. (1983) Arecibo radar observations of Comets IRAS-Araki-Alcock and Sugano-Saigusa-Fujikawa (abstract). *Bull. Am. Astron. Soc., 15,* 800.

Campbell D. B., Harmon J. K., and Shapiro I. I. (1989) Radar observations of Comet Halley. *Astrophys. J., 338,* 1094–1105.

Campbell M. J. and Ulrichs J. (1969) Electrical properties of rocks and their significance for lunar radar observations. *J. Geophys. Res., 74,* 5867–5881.

Campins H. (1988) The anomalous dust production in periodic comet Encke. *Icarus, 73,* 508–515.

Colwell J. E., Jakosky B. M., Sandor B. J., and Stern S. A. (1990) Evolution of topography on comets. II. Icy craters and trenches. *Icarus, 85,* 205–215.

Combi M. R. (1994) The fragmentation of dust in the innermost comae of comets: Possible evidence from ground-based images. *Astron. J., 108,* 304–312.

Crifo J. F. (1995) A general physicochemical model of the inner coma of active comets. I. Implications of spatially distributed gas and dust production. *Astrophys. J., 445,* 470–488.

de Pater I., Palmer P., Mitchell D. L., Ostro S. J., Yeomans D. K., and Snyder L. E. (1994) Radar aperture synthesis observations of asteroids. *Icarus, 111,* 489–502.

Epifani E., Colangeli L., Fulle M., Brucato J. R., Bussoletti E., De Sanctis M. C., Mennella V., Palomba E., Palumbo P., and Rotundi A. (2001) ISOCAM imaging of comets 103P/Hartley 2 and 2P/Encke. *Icarus, 149,* 339–350.

Fernández Y. R., Lisse C. M., Kundu A., A'Hearn M. F., Hoffman W. F., and Dayal A. (1996) The nucleus of Comet Hyakutake (abstract). *Bull. Am. Astron. Soc., 28,* 1088.

Fernández Y. R., Lisse C. M., Käufl H. U., Peschke S. B., Weaver H. A., A'Hearn M. F., Lamy P. P., Livengood T. A., and Kostiuk T. (2000) Physical properties of the nucleus of comet 2P/Encke. *Icarus, 147,* 145–160.

Fernández Y. R., Lowry S. C., Weissman P. R., and Meech K. J. (2002) New dominant periodicity in photometry of comet Encke (abstract). *Bull. Am. Astron. Soc., 34,* 887.

Finson M. L. and Probstein R. F. (1968) A theory of dust comets. I. Model and equations. *Astrophys J., 154,* 327–352.

Fulle M. (1990) Meteoroids from short period comets. *Astron. Astrophys., 230,* 220–226.

Fulle M. (1997) Injection of large grains into orbits around comet nuclei. *Astron. Astrophys., 325,* 1237–1248.

Fulle M., Mikuz H., and Bosio S. (1997) Dust environment of Comet Hyakutake 1996B2. *Astron. Astrophys., 324,* 1197–1205.

Giorgini J. D. (2002) Small-body astrometric radar observations [online]. California Institute of Technology, Pasadena [cited Oct. 1, 2002]. Available on line at http://ssd.jpl.nasa.gov/radar/data.html.

Goldstein R. M., Jurgens R. F., and Sekanina Z. (1984) A radar study of Comet IRAS-Araki-Alcock 1983d. *Astron. J., 89,* 1745–1754.

Gombosi T. I., Nagy A. F., and Cravens T. E. (1986) Dust and neutral gas modeling of the inner atmospheres of comets. *Rev. Geophys., 24,* 667–700.

Hallikainen M. T., Ulaby F. T., and Abdelrazik M. (1986) Dielectric properties of snow in the 3 to 37 GHz range. *IEEE Trans. Ant. Prop., AP-34,* 1329–1339.

Hanner M. S. (1981) On the detectability of icy grains in the comae of comets. *Icarus, 47,* 342–350.

Hanner M. S., Aitken D. K., Knacke R., McCorkle S., Roche P. F., and Tokunaga A. T. (1985) Infrared spectrophotometry of Comet IRAS-Araki-Alcock (1983d): A bare nucleus revealed? *Icarus, 62,* 97–109.

Hanner M. S., Newburn R. L., Spinrad H., and Veeder G. J. (1987) Comet Sugano-Saigusa-Fujikawa (1983V) — A small, puzzling comet. *Astron. J., 94,* 1081–1087.

Harmon J. K. (2002) Planetary delay-Doppler radar and the long-code method. *IEEE Trans. Geosci. Remote Sensing, 40,* 1904–1916.

Harmon J. K., Campbell D. B., Hine A. A., Shapiro I. I., and Marsden B. G. (1989) Radar observations of Comet IRAS-Araki-Alcock 1983d. *Astrophys. J., 338,* 1071–1093.

Harmon J. K. and 15 colleagues (1997) Radar detection of the nucleus and coma of Comet Hyakutake (C/1996 B2). *Science, 278,* 1921–1924.

Harmon J. K., Campbell D. B., Ostro S. J., and Nolan M. C. (1999) Radar observations of comets. *Planet. Space Sci., 47,* 1409–1422.

Harris W. M., Combi M. R., Honeycutt R. K., Mueller B. E. A., and Scherb F. (1997) Evidence of interacting gas flows and an extended volatile source distribution in the coma of Comet C/1996 B2 (Hyakutake). *Science, 277,* 676–681.

Hudson R. S. and Ostro S. J. (1995) Shape and non-principal axis spin state of asteroid 4179 Toutatis. *Science, 270,* 84–86.

Jenniskens P. and 13 colleagues (2002) Dust trails of 8P/Tuttle and the unusual outbursts of the Ursid shower. *Icarus, 159,* 197–209.

Jewitt D. C. and Luu J. (1992) Submillimeter continuum emission from comets. *Icarus, 100,* 187–196.

Jewitt D. C. and Matthews H. E. (1997) Submillimeter continuum observations of Comet Hyakutake (1996 B2). *Astron. J., 113,* 1145–1151.

Jewitt D. C. and Matthews H. E. (1999) Particulate mass loss from Comet Hale-Bopp. *Astron. J., 117,* 1056–1162.

Jorda L. and Rickman H. (1995) Comet P/Wirtanen, summary of observational data. *Planet. Space Sci., 43,* 575–579.

Jorda L., Lamy P., Groussin O., Toth I., A'Hearn M. F., and Peschke S. (2000) ISOCAM observations of cometary nuclei. In *ISO Beyond Point Sources: Studies of Extended Infrared Emission,* p. 61. ESA SP-455, Noordwijk, The Netherlands.

Kamoun P. G. D. (1983) Radar observations of cometary nuclei. Ph.D. thesis, Massachusetts Institute of Technology, Cam-

bridge. 273 pp.
Kamoun P. G., Pettengill G. H., and Shapiro I. I. (1982a) Radar detectability of comets. In *Comets* (L. L. Wilkening, ed.), pp. 288–296. Univ. of Arizona, Tucson.
Kamoun P. G., Campbell D. B., Ostro S. J., Pettengill G. H., and Shapiro I. I. (1982b) Comet Encke: Radar detection of nucleus. *Science, 216,* 293–295.
Kamoun P., Campbell D., Pettengill G., and Shapiro I. (1999) Radar observations of three comets and detection of echoes from one: P/Grigg-Skjellerup. *Planet. Space Sci., 47,* 23–28.
Keller H. U. and Markiewicz W. J. (1991) KOSI? *Geophys. Res. Lett., 18,* 249–252.
Kührt E., Knollenberg J., and Keller H. U. (1997) Physical risks of landing on a comet nucleus. *Planet. Space Sci., 45,* 665–680.
Lamy P. L., Toth I., Jorda L., Weaver H. A., and A'Hearn M. F. (1998) The nucleus and inner coma of Comet 46P/Wirtanen. *Astron. Astrophys., 335,* L25–L29.
Lamy P. L., Toth I., A'Hearn M. F., and Weaver H. A. (1999) Hubble Space Telescope observations of the nucleus of comet 45P/Honda-Mrkos-Pajdušáková and its inner coma. *Icarus, 140,* 424–438.
Lamy P. L., Toth I., A'Hearn M. F., Weaver H. A., and Weissman P. R. (2001) Hubble Space Telescope observations of the nucleus of comet 9P/Tempel 1. *Icarus, 154,* 337–344.
Levison H. F. and Duncan M. J. (1997) From the Kuiper Belt to the Jupiter-family comets: The spatial distribution of ecliptic comets. *Icarus, 127,* 13–32.
Licandro J., Tancredi G., Lindgren M., Rickman H., and Gil R. (2000) CCD photometry of cometary nuclei, I: Observation from 1990–1995. *Icarus, 147,* 161–179.
Lisse C. M., Fernández Y. R., Kundu A., A'Hearn M. F., Dayal A., Deutsch L. K., Fazio G. G., Hora J. L., and Hoffman W. F. (1999) The nucleus of comet Hyakutake (C/1996 B2). *Icarus, 140,* 189–204.
Luu J. and Jewitt D. (1990) The nucleus of Comet P/Encke. *Icarus, 86,* 69–81.
Magri C., Ostro S. J., Rosema K. D., Thomas M. L., Mitchell D. L., Campbell D. B., Chandler J. F., Shapiro I. I., Giorgini J. D., and Yeomans D. K. (1999) Mainbelt asteroids: Results of Arecibo and Goldstone radar observations of 37 objects during 1980–1995. *Icarus, 140,* 379–407.
Magri C., Consolmagno G. J., Ostro S. J., Benner, L. A. M., and Beeney B. R. (2001) Radar constraints on asteroid regolith properties using 433 Eros as ground truth. *Meteoritics & Planet. Sci., 36,* 1697–1709.
Marsden B. G. (1998) *Comet C/1998 K5 (LINEAR).* IAU Circular No. 6923.
McDonnell J. A. M. and 27 colleagues (1986) Dust density and mass distribution near Comet Halley from Giotto observations. *Nature, 321,* 338–341.
Meech K. J. and 11 colleagues (2002) Deep Impact — Exploring the interior of a comet. In *A New Era in Bioastronomy* (G. Lemarchand and K. Meech, eds.), pp. 235–242. Astronomical Society of the Pacific, San Francisco, California.
Mitchell D. L., Ostro S. J., Rosema K. D., Hudson R. S., Campbell D. B., Chandler J. F., and Shapiro I. I. (1995) Radar observations of asteroids 7 Iris, 9 Metis, 12 Victoria, 216 Kleopatra, and 654 Zelinda. *Icarus, 118,* 105–131.
Nolan M. C., Howell E. S., Harmon J. K., Campbell D. B., Margot J.-L., and Giorgini J. D. (2001) Arecibo radar observations of C/2001A2(B) (LINEAR) (abstract). *Bull. Am. Astron. Soc., 33,* 1120–1121.
Ostro S. J., Campbell D. B., Chandler J. F., Hine A. A., Hudson R. S., Rosema K. D., and Shapiro I. I. (1991a) Asteroid 1986 DA: Radar evidence for a metallic composition. *Science, 252,* 1399–1404.
Ostro S. J., Campbell D. B., Chandler J. F., Shapiro I. I., Hine A. A., Velez R., Jurgens R. F., Rosema K. D., Winkler R., and Yeomans D. K. (1991b) Asteroid radar astrometry. *Astron. J., 102,* 1490–1502.
Ostro S. J. and 13 colleagues (1995) Radar images of asteroid 4179 Toutatis. *Science, 270,* 80–83.
Ostro S. J. and 15 colleagues (1996) Near-Earth object radar astronomy at Goldstone in 1996 (abstract). *Bull. Am. Astron. Soc., 28,* 1105.
Ostro S. J., Nolan M. C., Margot J.-L., Magri C., Harris A. W., and Giorgini J. D. (2001) Radar observations of asteroid 288 Glauke. *Icarus, 152,* 201–204.
Ostro S. J., Hudson R. S., Benner L. A. M., Giorgini J. D., Magri C., Margot J.-L., and Nolan M. C. (2002) Asteroid radar astronomy. In *Asteroids III* (W. F. Bottke Jr. et al., eds.), pp. 151–168. Univ. of Arizona, Tucson.
Reach W. T., Sykes M. V., Lien D., and Davies J. K. (2000) The formation of Encke meteroids and dust trail. *Icarus, 148,* 80–94.
Richter K. and Keller H. U. (1995) On the stability of dust particle orbits around comet nuclei. *Icarus, 114,* 355–371.
Samarasinha N. H. and A'Hearn M. F. (1991) Observational and dynamical constraints on the rotation of comet P/Halley. *Icarus, 93,* 194–225.
Samarasinha N. H., Mueller B. E. A., Belton M. J. S., and Jorda L. (2004) Rotation of cometary nuclei. In *Comets II* (M. C. Festou et al., eds.), this volume. Univ. of Arizona, Tucson.
Sarmecanic J., Fomenkova M., Jones B., and Lavezzi T. (1997) Constraints on the nucleus and dust properties from mid-infrared imaging of Comet Hyakutake. *Astrophys. J. Lett., 483,* L69–L72.
Schleicher D. G. and Osip D. J. (2002) Long- and short-term photometric behavior of Comet Hyakutake (1996 B2). *Icarus, 159,* 210–233.
Schleicher D. G., Millis R. L., Osip D. J., and Lederer S. M. (1998) Activity and the rotation period of comet Hyakutake (1996 B2). *Icarus, 131,* 233–244.
Sekanina Z. (1988) Nucleus of Comet IRAS-Araki-Alcock (1983 VII). *Astron. J., 95,* 1876–1894.
Sekanina Z., Jehin E., Boehnhardt H., Bonfils X., and Schuetz O. (2002) Recurring outbursts and nuclear fragmentation of comet C/2001 A2 (LINEAR). *Astrophys. J., 572,* 679–684.
Skorov Y. V. and Rickman H. (1999) Gas flow and dust acceleration in a cometary Knudsen layer. *Planet. Space Sci., 47,* 935–949.
Veverka J. and 32 colleagues (2000) NEAR at Eros: Imaging and spectral results. *Science, 289,* 2088–2097.
Wallis M. K. (1982) Dusty gas dynamics in real comets. In *Comets* (L. L. Wilkening, ed.), pp. 357–369. Univ. of Arizona, Tucson.
Weissman P. R., Asphaug E., and Lowry S. C. (2004) Structure and density of cometary nuclei. In *Comets II* (M. C. Festou et al., eds.), this volume. Univ. of Arizona, Tucson.
Whipple F. L. (1951) A comet model: II. Physical relations for comets and meteors. *Astrophys. J., 113,* 464–474.
Wilkening L. L., ed. (1982) *Comets*. Univ. of Arizona, Tucson. 766 pp.
Yeomans D. K., Chodas P. W., Keesey M. S., Ostro S. J., Chandler J. F., and Shapiro I. I. (1992) Asteroid and comet orbits using radar data. *Astron. J., 103,* 303–317.